Midinfrared Hall effect in thin-film metals: Probing the Fermi surface anisotropy in Au and Cu

J. Černe,* D. C. Schmadel, M. Grayson, G. S. Jenkins, J. R. Simpson, and H. D. Drew
Center for Superconductivity Research and Department of Physics, University of Maryland, College Park, Maryland 20741
(Received 21 July 1999)

A sensitive midinfrared (MIR, 900–1100 cm^{-1}, 112–136 meV) photoelastic polarization modulation technique is used to measure simultaneously Faraday rotation and circular dichroism in thin metal films. These two quantities determine the complex ac Hall conductivity. This technique is applied to study Au and Cu thin films at temperatures in the range (300 K $>T>$ 20 K), and magnetic fields up to 8 T. The Hall frequency ω_H is consistent with band theory predictions. We report a measurement of the MIR Hall scattering rate γ_H which is significantly lower than that derived from Drude analysis of zero magnetic field MIR transmission measurements. This difference is qualitatively explained in terms of the anisotropy of the Fermi surface in Au and Cu.

I. INTRODUCTION

The dc Hall effect is a standard tool for the study of electronic properties of conducting materials. In the high-field limit ($\omega_c\tau \gg 1$, where ω_c is the cyclotron frequency and τ is the carrier scattering time) it can be shown that the Hall coefficient $R_H (R_H \propto 1/n)$ can give the number density n of carriers. In many electronic materials, however, because of the combination of large effective masses $m(\omega_c \propto 1/m)$ and short defect-induced carrier scattering times τ, it is not possible to achieve the high-field limit of the Hall effect. Under these conditions the Hall effect is sensitive to the details of electronic defect scattering in the sample, which complicates its interpretation. Also, in many of these interesting materials, electron interactions are strong and the Fermi-liquid theory conditions that are assumed in transport theory are possibly not met. Nevertheless, the dc Hall effect has provided interesting and important information on these materials.[1] The ac Hall effect offers the possibility of overcoming some of the limitations of the dc Hall effect while providing additional information on the electronic structure of materials. While dc transport can be shown to be mainly sensitive to the mean free path of the carriers,[2] ac transport is sensitive to the energy scales of the system: the plasma frequency, the cyclotron frequency, and the carrier relaxation rates. At sufficiently high frequencies $\omega \gg \frac{1}{\tau}$ the ac conductivity becomes insensitive to the impurity scattering, thereby giving information about the intrinsic electronic structure of the system. It can provide insight into the physics of systems ranging from conventional Fermi-liquid metals to more exotic metals such as high-temperature superconductors[3] and other transition-metal oxides.[4]

Within Fermi-liquid theory and the relaxation-time approximation, and assuming cubic symmetry, the conductivity tensor can be expressed as integrals over the Fermi surface (FS);[5]

$$\sigma_{xx} = \frac{e^2}{(2\pi)^3 \hbar} \oint_{FS} dS |\mathbf{v}(k)| \tilde{\tau}(k), \tag{1.1a}$$

$$\sigma_{xy} = \frac{e^3 B}{(2\pi)^3 \hbar^2 c} \oint_{FS} dS \mathbf{e}_z \cdot \left[\mathbf{v}(k) \tilde{\tau}(k) \times \frac{d[\mathbf{v}(k)\tilde{\tau}(k)]}{dk} \right], \tag{1.1b}$$

where $\mathbf{v}$ is the carrier velocity; k is the carrier momentum; $\tilde{\tau} = \tau/(1 - i\omega\tau)$, where τ is the scattering time at point k on the FS; B is the magnetic field; e is the electron charge; $\hbar$ is Planck's constant; c is the speed of light; and $\mathbf{e}_z$ is the unit vector along the z axis ($\mathbf{B} \| \mathbf{z}$). Since σ_{xy} depends on the cross product $\mathbf{v} \times \mathbf{dv}$, flat regions of the FS (where $dv = 0$) do not contribute to σ_{xy}, whereas high curvature regions, which can produce large angular differences between $\mathbf{v}$ and $\mathbf{dv}$, will be heavily weighted in the integral in Eq. (1.1b).

In the study of the ac Hall effect, the complex Hall angle θ_H is a particularly useful quantity. θ_H is defined as

$$\tan \theta_H = \frac{\sigma_{xy}}{\sigma_{xx}}, \tag{1.2}$$

where σ_{xx} and σ_{xy} are the diagonal and off-diagonal components of the complex magnetoconductivity tensor. Note that $\tan \theta_H$ is independent of film thickness d, which is useful since d may not be accurately known. For a simple (Drude) metal, $\tan \theta_H$ reduces to $\omega_c \tau$ in the dc limit. θ_H has proven to be especially interesting in high-temperature superconductors where the scattering rate associated with θ_H shows striking qualitative and quantitative differences from the rate associated with σ_{xx}. This behavior has been cited as evidence for non-Drude and even non-Fermi-liquid physics for high-temperature superconductors in the normal state.[6–8] Interesting differences in scattering rates can also be found in more conventional materials such as Au and Cu, as will be explored in this paper.

In general $\tan \theta_H$, as the ratio of two response functions, is a complicated function which does not have a simple closed form. The simplest generalization of θ_H to finite frequency is[9]

$$\tan \theta_H = \frac{\omega_H}{\gamma_H - i\omega} \approx \theta_H, \tag{1.3}$$

where ω_H is the Hall frequency and γ_H is the Hall scattering rate. In this experiment, since ω_H is small compared to ω and γ_H, we will use the approximation $\tan\theta_H \approx \theta_H$ throughout this paper. Equation (1.3) is valid for a Drude metal, in which case, $\omega_H = \omega_c$ and $\gamma_H = \gamma_{xx}$, where ω_c and γ_{xx} are the conventional cyclotron frequency and the isotropic Drude scattering rate, respectively. Equation (1.3) is also valid for Fermi liquids for the case of a *k*-independent scattering time. Furthermore, it is the form obtained in several proposed models of the normal state transport in high-temperature superconductors.[6–8]

Although σ_{xy} and θ_H tend to be small for metals in the midinfrared (MIR) (900–1100 cm^{-1}), there are a number of advantages in performing these higher-frequency measurements. First, the high frequency allows one to avoid impurity scattering or grain boundary effects which may dominate lower frequency Hall measurements. This is especially important in new materials which often contain many impurities and defects. Thus the MIR measurements can probe intrinsic optical properties more directly. Furthermore, MIR measurements allow one to examine the trends observed at lower frequencies. Since $\tan\theta_H$ (and θ_H) obeys a sum rule [see Eq. (A1)],[10] it is very useful to be able to integrate θ_H to higher frequencies to verify whether (and where) the Hall angle sum rule saturates or whether there is more relevant physics at even higher frequencies. Finally, since the high frequency behavior of θ_H is constrained by the general requirements of response functions, the asymptotic form for θ_H in Eqs. (1.3) and (A10) becomes more accurate at higher frequencies.

In this paper, we examine the MIR Hall effect in Au and Cu thin films. We introduce a sensitive photoelastic polarization modulation technique in Sec. II A. Section II B describes the samples. Section III presents MIR magneto-optic transmission measurements from 900 to 1100 cm^{-1}. We determine the complex conductivity tensor σ at temperatures from 20 to 300 K, and magnetic fields up to $8T$. The resulting Hall frequency ω_H is in good agreement with band theory, while the scattering rate γ_H determined from the Hall angle is significantly lower than the scattering rate γ_{xx} measured in zero-magnetic-field transmittance measurements. Section IV A presents a qualitative model that is used to discuss these results in terms of the anisotropy of the FS of Au and Cu. Section IV B compares the results for the MIR measurements with dc results. The Appendix provides theoretical background for the infrared transport functions that are used to analyze the experimental data.

II. EXPERIMENT

A. Polarimetry measurements

Since $\omega_H \ll (\gamma_H, \omega)$ and since at high frequencies $\mathrm{Re}[\theta_H] \propto \omega^{-2}$ and $\mathrm{Im}[\theta_H] \propto \omega^{-1}$ [see Eq. (1.3)], the MIR θ_H in metals is small, on the order of 10^{-3} rad. Therefore, a sensitive technique is required for the MIR θ_H measurements. In the MIR we measure the complex Faraday angle θ_F, which is the optical analog of θ_H. θ_F is defined as

$$\theta_F = \frac{t_{xy}}{t_{xx}}, \tag{2.1}$$

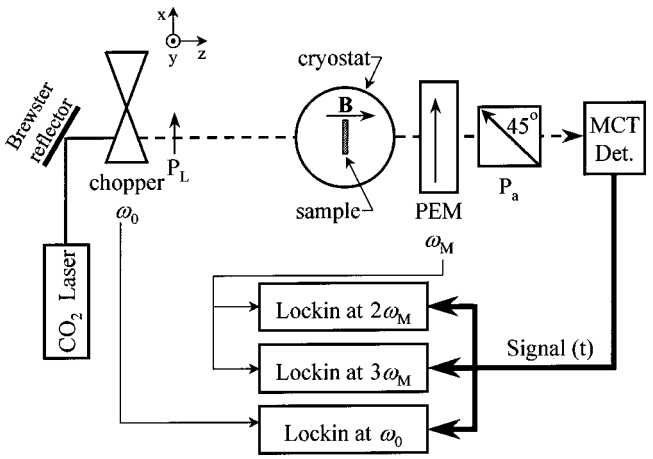

FIG. 1. A schematic of the experimental setup.

where t_{xx} and t_{xy} are the complex transmission amplitudes. In the thin-film approximation, the relationship between θ_F and θ_H is given by

$$\theta_F \approx \tan\theta_F = \frac{t_{xy}}{t_{xx}} \approx \frac{\dfrac{4nZ\sigma_{xy}}{(1+Z\sigma_{xx})^2}}{\dfrac{4n}{1+Z\sigma_{xx}}} = \left(1+\frac{1}{Z\sigma_{xx}}\right)\theta_H,$$

$$Z = \frac{Z_0 d}{n+1}, \tag{2.2}$$

where Z_0 is the impedance of free space, n is the substrate index of refraction, and d is the film thickness. As with θ_H, the small-angle approximation applies to θ_F in this experiment, so $\tan\theta_F \approx \theta_F$. The experimental data are actually analyzed using finite thickness film calculations, which deviate from the thin film results by less than 10%. Furthermore, since the conductances ($\sigma_{xx}d$) of Au and Cu films are large, $1/Z\sigma_{xx} \ll 1$ so $\theta_H \approx \theta_F$. However, in this paper, σ_{xx} is determined through zero-magnetic-field transmittance measurements, and these corrections (less than 15%) are included in calculating θ_H and σ_{xy} from θ_F.

Figure 1 shows the experimental setup for measuring θ_F. A CO_2 laser produces linearly polarized MIR radiation in the range 9–11 μm (1100–900 cm^{-1} and 112–136 meV). First, a conventional optical chopper modulates this radiation at ω_0 (80–150 Hz). In this schematic, the laser polarization P_L is along $\hat{x}$. In the Faraday geometry, the radiation then passes through the sample which is located at the center of an 8-T magneto-optical cryostat. In order to sensitively measure both the real and imaginary parts of θ_F, the radiation that is transmitted by the sample is analyzed using a photoelastic modulator (PEM).[11] The PEM periodically retards the phase of one linear polarization component $E_x\hat{x}$ with respect to the orthogonal component $E_y\hat{y}$ as follows:

$$E_x\hat{x} + E_y\hat{y} \rightarrow E_x e^{i\Delta(t)}\hat{x} + E_y\hat{y}. \tag{2.3}$$

$\Delta(t)$ is the sinusoidal phase modulation of $E_x\hat{x}$ with respect to $E_y\hat{y}$, and is given by

$$\Delta(t) = \beta\cos(\omega_M t), \quad \beta = \frac{\Delta n 2\pi D}{\lambda}, \tag{2.4}$$

where β is the phase modulation amplitude, Δn is the difference between the indices of refraction in the x and y directions, D is the optical path length in the PEM, λ is the wavelength of the radiation, and ω_M is the PEM modulation frequency (50 kHz). Since the sample is axially symmetric along B, the transmittance tensor is diagonal when represented in the circular polarization basis. Therefore, changes in the incident linearly polarized light depend only on (1) the relative difference in the phase of left versus right circularly polarized light due to $\mathrm{Re}[\theta_F]$, which leads to a rotation of the polarization axis [Faraday rotation-(FR)]; and (2) the relative difference in the transmission of left versus right circularly polarized light due to $\mathrm{Im}[\theta_F]$, which introduces ellipticity [circular dichroism-(CD)] to the beam. The optical axis of the PEM is oriented parallel to that of the laser radiation along $\hat{x}$, so that no modulation occurs unless the sample produces a $\hat{y}$ component in the polarization by either rotating the polarization (FR) or introducing ellipticity to the polarization (CD). Finally, a static linear polarizer P_a selects the component of the radiation at 45° to $\hat{x}$. A liquid-nitrogen-cooled mercury-cadmium-telluride (MCT) element detects the radiation, and three lock-in amplifiers demodulate the resulting time-dependent signal. Combining a bright source such as a CO_2 laser with a sensitive MCT detector provides a signal-to-detector noise level of up to 10^5. The high sensitivity is especially important due to the low transmittance ($<$ 3%) of the samples used in this experiment. The signal intensity is kept within the linear response regime of the MCT detector.

The FR ($\mathrm{Re}[\theta_F]$) and CD ($\mathrm{Im}[\theta_F]$) signals are related to the even and odd harmonics of ω_M, respectively. These harmonic signals can be normalized by the average signal chopped at ω_0 to obtain, for small θ_F:

$$\frac{I_{2\omega_M}}{I_{\omega_0}} = \frac{4J_2(\beta)\mathrm{Re}[\theta_F]}{1+|\theta_F|^2-2\mathrm{Re}[\theta_F]J_0(\beta)}, \tag{2.5a}$$

$$\frac{I_{3\omega_M}}{I_{\omega_0}} = \frac{4J_3(\beta)\mathrm{Im}[\theta_E]}{1+|\theta_F|^2-2\mathrm{Re}[\theta_F]J_0(\beta)}, \tag{2.5b}$$

where $I_{n\omega_M}$, $J_n(\beta)$, and I_{ω_0} are the intensity of the nth harmonic of ω_M, the nth-order Bessel function, and the average intensity chopped at ω_0, respectively. Since $|\theta_F|^2 \ll 1$ and β is chosen so that $J_0(\beta)=0$, the denominators in Eqs. (2.5a) and (2.5b) are unity. The $3\omega_M$ harmonic signal is chosen in Eq. (2.5b) over the fundamental frequency in order to avoid background signals (such as electrical pickup and interference modulation) that occur at ω_M. With this technique one can simultaneously measure both the real and imaginary parts of θ_F with a sensitivity of approximately one part in 10^4 and 4×10^3, respectively. The difference in sensitivity for the real and imaginary parts of θ_F is mainly due to the fact that at a typical PEM retardance $\beta \approx 2.39$ rad, and $J_2(\beta) \approx 2\times J_3(\beta)$. The great stability of the measurement is due in part to using a single detector to measure all the signals simultaneously, so that the detector and source drift can be accurately normalized out.

Although all the parameters in Eqs. (2.5a) and (2.5b) are measured independently, the calibration of the system is verified by removing the sample and rotating a quarter-waveplate in front of the optical magnet shown in Fig. 1. The signals as a function of quarter-waveplate orientation angle are consistent with predictions from the initial calibration. For more details on this measurement technique, see Ref. 12.

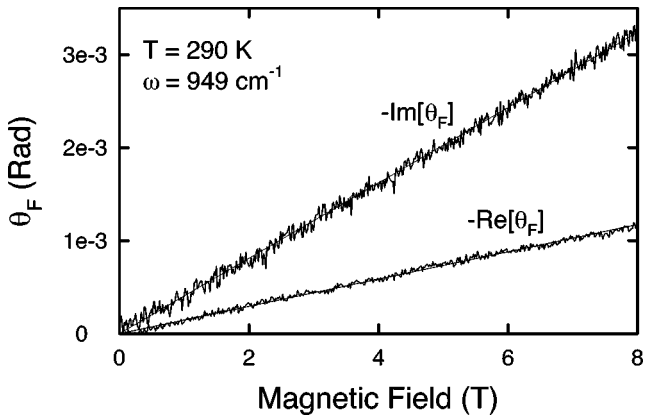

FIG. 2. The complex Faraday angle θ_F for a Cu film as a function of magnetic field at 949 cm^{-1} and 290 K.

B. Samples

The samples consist of thin Au and Cu films grown on semiconductor substrates using conventional vacuum thermal deposition techniques. The film thicknesses are on the order of 10 nm, corresponding to dc sheet resistances in the range of $R_\square \approx 6-10\ \Omega$. The thickness is chosen to maximize the quality of the film and the magneto-optic signals while maintaining a transmittance of approximately 5% at 1000 cm^{-1}. Substrates consist of 0.5-mm-thick insulating Si($\rho \geqslant 2000\ \Omega\,\mathrm{cm}$) or GaAs. The dc residual resistance ratio ($R_{300\,K}/R_{10\,K}$) for the Au and Cu films is 1.6 and 1.3, respectively. It is well known that noble-metal thin films grown by thermal evaporation on unheated substrates produce polycrystalline films with grain sizes comparable with the film thickness.[13] The low-temperature resistance of the films is dominated by interface scattering, as will be shown in Sec. IV A. Since interference (etalon) effects associated with the substrate can have a strong effect on FR and CD measurements, the substrates are either wedged 1° to remove multiply reflected beams or coated with a NiCr broadband antireflection coating.[14] An antireflection coating with $R_\square = 157\ \Omega$ for Si and $R_\square = 149\ \Omega$ for GaAs reduces the etalon interference fringes to less than 5% of the transmittance signal.

III. RESULTS

Figure 2 shows $\mathrm{Re}[\theta_F]$ and $\mathrm{Im}[\theta_F]$ [see Eqs. (2.5a) and (2.5b)] as functions of magnetic field B at room temperature for a Cu sample. The MIR radiation frequency is 949 cm^{-1}. The substrate's background contribution to $\mathrm{Re}[\theta_F]$ has been removed. Although both Si and GaAs substrates produce signicant $\mathrm{Re}[\theta_F]$ signal ($\approx 2-3\times10^{-3}$ rad, respectively), their contribution to $\mathrm{Im}[\theta_F]$ is negligible. Both signals are linear in B, as expected.

Figure 3 shows the temperature dependence of θ_H (a) and θ_H^{-1} (b) at 1079 cm^{-1} and 8 T for a Au sample. The solid (empty) circles represent the real (imaginary) part of θ_H and

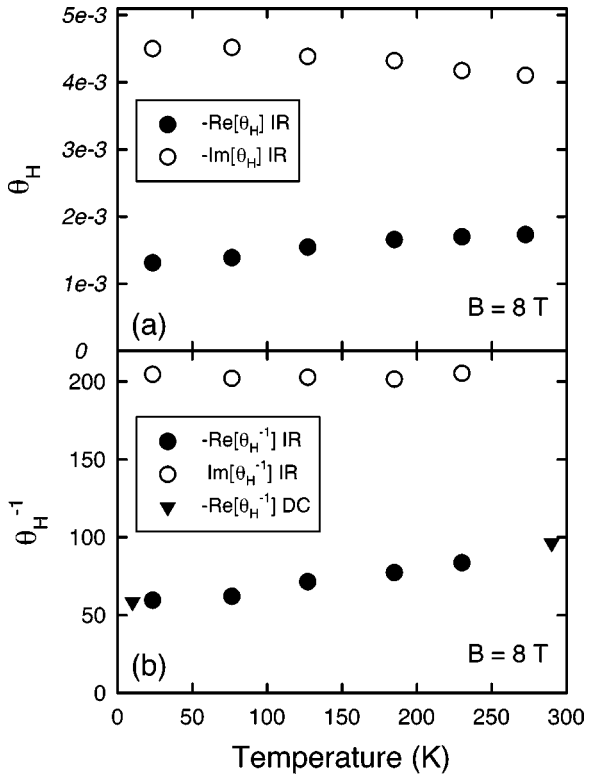

FIG. 3. The complex Hall angle θ_H (a) and inverse Hall angle θ_H^{-1} (b) for Au as functions of temperature at 1079 cm^{-1} and 8 T. The solid (empty) circles correspond to the real (imaginary) part of θ_H and θ_H^{-1} in the MIR. The solid triangles in (b) show the dc values for θ_H^{-1}.

θ_H^{-1}. Note that $\mathrm{Im}[\theta_H]$ is greater than $\mathrm{Re}[\theta_H]$ by approximately a factor of 4, which suggests that the measurement is approaching the high-frequency regime where $\mathrm{Im}[\theta_H] \gg \mathrm{Re}[\theta_H]$. Although both $\mathrm{Re}[\theta_H]$ and $\mathrm{Im}[\theta_H]$ show weak temperature dependences in Fig. 3(a), only $\mathrm{Re}[\theta_H^{-1}]$ shows a temperature dependence in Fig. 3(b). This is consistent with a temperature-dependent γ_H and temperature-independent ω_H [see Eqs. (1.3) and (A10)]. The solid triangles in Fig. 3(b) show the dc θ_H^{-1} at low and high temperatures. The dc R_H measurements are made using Van der Pauw geometry on the same thin film samples that are examined in the MIR. The dc θ_H^{-1} is seen to agree well with the MIR $\mathrm{Re}[\theta_H^{-1}]$.

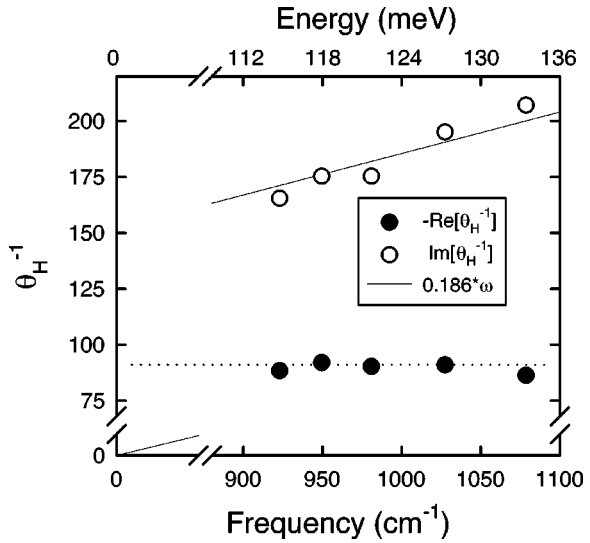

FIG. 4. The complex inverse Hall angle θ_H^{-1} for Au is shown as a function of frequency at 290 K and 8 T. The solid (empty) circles represent the real (imaginary) part of θ_H^{-1}. $\mathrm{Re}[\theta_H^{-1}]$ shows no frequency dependence, while the empty circles representing $\mathrm{Im}[\theta_H^{-1}]$ show a linear temperature dependence, as expected from Eq. (A10).

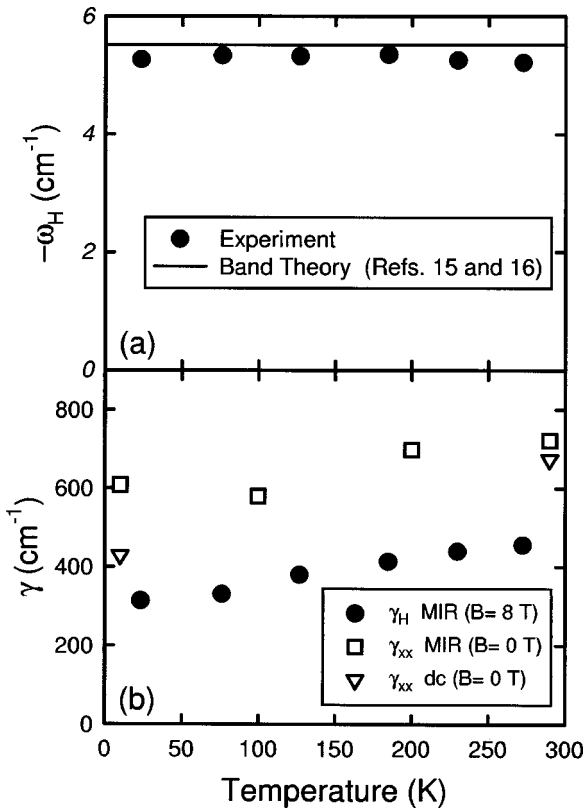

FIG. 5. The Hall frequency ω_H (a) and Hall scattering rate γ_H (b) for Au as functions of temperature at 1079 cm^{-1} and 8 T. ω_H is independent of temperature and agrees well with the prediction from band calculations, which is shown by the solid line in (a). MIR γ_H at 8 T (solid circles), MIR γ_{xx} (empty squares), and dc γ_{xx} (empty triangles) are shown in (b). Despite large differences in magnitude, these scattering rates show similar temperature dependences.

Figure 4 shows the frequency dependence of θ_H^{-1} at 290 K and 8 T. $\mathrm{Im}[\theta_H^{-1}]$, which is represented by empty circles which show a linear increase with frequency, suggesting a frequency independent ω_H [see Eq. (A10)]. The $\mathrm{Im}[\theta_H^{-1}]$ data are fitted with a line intersecting the origin, whose slope agrees with band predictions to within 2%. $\mathrm{Re}[\theta_H^{-1}]$ is represented by solid circles and shows no frequency dependence corresponding to a frequency independent of γ_H.

Figure 5 shows the temperature dependence of the Hall frequency ω_H and Hall scattering rate γ_H at 8 T. ω_H shows no temperature dependence in Fig. 5(a), and agrees well with the value obtained using band theory (solid line).[15,16] Figure 5(b) shows the MIR γ_H at 8 T (solid circles), the MIR γ_{xx} (empty squares), and the dc γ_{xx} (empty triangles). The MIR γ_{xx} is obtained from zero-field transmittance spectra (1000–7000 cm^{-1}). These spectra are measured using a Fourier transform spectrometer. The data are fitted with a simple Drude model to obtain the MIR σ_{xx} and γ_{xx}, which are used

TABLE I. Comparison of the Hall scattering rates γ_H and γ_{xy} [see Eq. (A12a)] obtained from magneto-optic measurements with the longitudinal scattering rate γ_{xx} obtained from a Drude fit to zero-magnetic-field transmission measurements. Note the strong anisotropy between γ_H and γ_{xx}. All measurements are performed at 290 K.

Sample	Frequency (cm^{-1})	γ_H (cm^{-1})	γ_{xy} (cm^{-1})	γ_{xx} (cm^{-1})	γ_{xy}/γ_{xx}
Cu	949	525 ± 55	605 ± 60	685 ± 70	0.88
Au	1079	449 ± 45	585 ± 60	720 ± 76	0.81

to transform θ_F into θ_H. The DC γ_{xx} is determined from the dc resistivity which is measured using conventional four-probe electrical techniques. The MIR values for γ_{xx} are higher than those obtained using dc measurements, especially at lower temperatures. Though exhibiting a similar temperature dependence, γ_H are signifantly lower than both the MIR and dc γ_{xx}. Note that the scattering rates only decrease by 15–30 % at low temperature, which suggests that the scattering rate is dominated by the interfaces of the films (as is discussed in Sec. IV A).

Table I shows the Hall scattering rates γ_H and γ_{xy} along with the zero-field scattering rate γ_{xx}. Au films show a greater difference between γ_{xy} and γ_{xx} than the Cu film, with $\gamma_{xy}/\gamma_{xx}\approx 0.81$ for the former and 0.88 for the latter.

Table II shows the measured and predicted values for the Hall frequency. ω_H agrees well with predictions from band calculations.[15,16] For Cu, the measured ω_H is higher than, but within 10% of the predicted[15,16] Hall frequency ω_H^{band}. For Au the agreement is even better, with a variation of less than 5%. The linear fit in Fig. 4(a) produces a measured ω_H that is within 2% of the band calculated value for Au.

Table III shows the Hall coefficient $R_H=\sigma_{xy}/\sigma_{xx}^2$, from this and other experiments. R_H^{band} is derived from band calculations[15] while R_H^{free} assumes a spherical FS and reduces to the well-known formula for free electrons, $R_H^{\text{free}}=-1/nec$, where n is the electron density and c is the speed of light. R_H^{bulk} are from room temperature dc measurements on bulk samples.[17] Note that the MIR values for $\text{Re}[R_H]$ agree well with R_H^{band} for both Au and Cu. The MIR $\text{Im}[R_H]$ are approximately a factor of 5–8 times smaller than $\text{Re}[R_H]$ (see Sec. IV B). The dc R_H for Au agrees well with R_H^{free}, while the dc R_H for Cu agrees better with the MIR measured value than R_H^{free}. The MIR and dc measurements in both samples show little temperature dependence.

IV. DISCUSSION

The dc resistivity of bulk Au and Cu at 300 K is dominated by electron-phonon scattering. From the bulk resistivity and the known plasma frequency we can estimate the electron relaxation rate as 180 cm^{-1}, corresponding to a mean free path of about 42 nm. For frequencies above the Debye frequency the electron-phonon scattering is expected to be independent of frequency but larger than its dc value due to phonon emission processes. At zero temperature the effective IR relaxation rate due to phonons is $\gamma_{\text{eff}}=\frac{2}{5}(\Theta_D/T)\gamma_{\text{dc}}\approx 40\,cm^{-1}$, where Θ_D is the Debye temperature, and where γ_{dc} is the scattering rate at high temperature T.[18] In the observed γ_H, γ_{xx}(MIR), and γ_{xx}(dc) in Fig. 5, the temperature dependence is consistent with electron-phonon scattering but the total scattering is larger than γ_{eff}. Therefore, the relaxation rates in these thin films have contributions from other processes. Since the film thicknesses are of order 10 nm, we expect the boundary scattering of the electrons to be significant. Also, the absence of a frequency dependence of the γ's in Fig. 4 is consistent with this picture, and indicates that electron-electron scattering is weak in Au and Cu as expected.

TABLE II. Comparison of the Hall frequency ω_H with the ω_H^{band} predicted from band calculations (Refs. 15 and 16). The agreement is within the experimental error. All measurements are performed at 290 K.

Sample	Frequency (cm^{-1})	ω_H (cm^{-1})	ω_H^{band} (cm^{-1})	$\omega_H/\omega_H^{\text{band}}$
Cu	949	-4.1 ± 0.2	-3.8	1.08
Au	923	-5.6 ± 0.3	-5.5	1.02
Au	1079	-5.2 ± 0.3	-5.5	0.95

A. Anisotropic Fermi-surface model

In this section we will discuss the observed IR relaxation rates in terms of the scattering of the electrons at the boundaries of the films. We assume that experiment measures the conductivity tensor averaged uniformly over the Fermi surface of Au and Cu. Since the Hall angle is small ($\sim 10^{-3}$) the k-space paths are an infinitesimal fraction of a complete cyclotron orbit. The cubic symmetry implies that each Fermi-surface patch for each grain is sampled with many different field orientations. This alone would reduce any orientation dependence of the conductivity. Indeed it is well known that σ_{xx} is independent of orientation in a cubic material. In the case of polycrystalline films a further randomization comes from the averaging over the different orientations of the grains of the film. Also, since the measurements in these experiments occur at high frequencies, we are averaging the contributions of the different grains. This is not generally true in dc measurements where the response functions such as resistance can be dominated by a few domains

TABLE III. Comparison of the MIR and dc Hall coefficients R_H. The units for R_H are $10^{-11}\,m^3\,C^{-1}$. The Cu and Au MIR measurements are performed at 949 and 1079 cm^{-1}, respectively.

Sample	T (K)	MIR R_H	dc R_H	R_H^{band} (Ref. 15)	R_H^{free} (Ref. 15)	dc R_H^{bulk} (Ref. 17)
Cu	290	$-4.42-0.465i$	-4.28	-5.2	-7.3	-5.17
Cu	40	$-4.28-0.534i$	-4.75			
Au	290	$-8.04-1.49i$	-9.9	-8.1	-10.5	-7.16
Au	23	$-7.96-1.65i$	-10.4			

with the optimal orientation, which ''short out'' the contributions from the other less favorably aligned domains. Thus, we expect our results to reflect the calculated averages more accurately than dc measurements. Therefore, we believe that the assumption for σ_{xx} and σ_{xy} (i.e., that the experiment samples all possible electron orbits with all possible magnetic field orientations) is a good one.

The difference between γ_H and γ_{xx} is a consequence of anisotropic scattering on the FS. This is seen more clearly from Eqs. (A4a) and (A4b) for γ_{xx} and γ_{xy}. These quantities correspond to two different averages of the scattering over the FS. From Eq. (A4b) it is seen that γ_{xy} weights more heavily the regions of the FS with strong curvature.

A simple argument based on the FS anisotropy of Au and Cu can account for the difference between γ_{xy} and γ_{xx}. The anisotropy of the FS in Au and Cu is well characterized. The high curvature regions near the L point of the FS are referred to as necks, while the low curvature regions everywhere else are referred to as bellies. High curvature necks have a larger Hall conductivity σ_{xy} [see Eq. (1.1b)], while the lower curvature bellies, which make up a greater fraction of the FS, tend to dominate the longitudinal conductivity σ_{xx}.[6,7] Furthermore, the scattering rate of carriers in the necks can be different from those in the bellies, with γ_{xy} (γ_{xx}) tending to represent the characteristic scattering rate for carriers in the neck (belly). In bulk materials, the anisotropy in the scattering rate is due to the anisotropy of the electron-phonon interaction.[19,20] However, in thin films the scattering is dominated by the film interfaces and different mechanisms are responsible for the anisotropy. We explore one such mechanism, the anisotropy of the Fermi velocity v_F, in the rest of this section.

Since the bulk scattering length l_0 of the Au and Cu films at room temperature is roughly a factor of 4 greater than the thickness of these films, one expects the scattering length l_f in the films to be dominated by interface scattering. The ratio of the film conductivity σ_f and bulk conductivity σ_0 is given by[21]

$$\frac{\sigma_f}{\sigma_0} \approx \frac{3}{4}\frac{d}{l_0}\ln\left(\frac{l_0}{d}\right), \tag{4.1}$$

where d is the film thickness. The conductivity ratio that is measured in the Au (Cu) film is within 10% (30%) of the value predicted by Eq. (4.1), and suggests that the scattering length is dominated by the film thickness rather than impurities or phonons. Since the film consists of randomly oriented grains, and since l_f is independent of k, one expects the average scattering length to be isotropic along the FS and related only to the separation d between film interfaces as implied by Eq. (4.1). For simplicity, we take the scattering time τ to be related to the scattering length l_f and Fermi velocity v_F as follows:

$$l = v_F\tau \approx d. \tag{4.2}$$

The scattering rate γ can then be expressed as

$$\gamma(k) = \frac{1}{\tau(k)} = \frac{v_F(k)}{l_f}, \tag{4.3}$$

where $\gamma(k)$ and $\tau(k)$ are the scattering rate and scattering time of the carriers on the FS. From this simple argument, one can estimate that γ(neck) is related to γ(belly) as follows:

$$\frac{\gamma_{xy}}{\gamma_{xx}} \rightarrow \frac{\gamma(\text{neck})}{\gamma(\text{belly})} = \frac{v_F(\text{neck})}{v_F(\text{belly})} \approx 0.56\text{–}0.65, \tag{4.4}$$

where the values for v_F(neck) and v_F(belly) represent the typical extrema of v_F at the necks and bellies reported in Refs. 19 and 20. Since the Hall measurements involve contributions from both neck and belly regions, the anisotropy observed in the experiment should be smaller than that predicted by Eq. (4.4), which only involves extremal values of v_F. This can be seen in Table I. In fact, the results in Eq. (4.4) represent an upper limit of the anisotropy. For a more quantitative theoretical comparison, the FS integrals in Eqs. (A4a) and (A4b) need to be calculated.

B. Comparison of MIR and dc results

The frequency dependence of the values measured in this experiment provides important information about anisotropy and inelastic scattering. In this section, we will discuss the frequency dependence of R_H, θ_H^{-1}, and γ_{xx}. The Hall coefficient R_H is shown in Table III. For Au, the MIR value of Re$[R_H]$ is independent of frequency and temperature, and 20% lower than the dc value. Similar results are found for Cu, but with the low-temperature MIR R_H only 10% smaller than the dc value. This difference between the dc and MIR values for R_H implies anisotropic scattering on the FS (see the Appendix). The MIR values of R_H for Au and Cu are in good agreement with band calculations.[15] On the other hand, the dc value for Au for these films (in contrast to the dc R_H^{bulk}) gives the correct carrier density, presumably fortuitously. The MIR Im$[R_H]$ is nonzero for both Au and Cu, with magnitudes of 20% and 12% of the R_H, respectively. A nonzero Im$[R_H]$ occurs only for a frequency-dependent Re$[R_H]$, and the magnitude of Im$[R_H]$ is related to the difference between the dc and MIR Re$[R_H]$. Therefore, the larger Im$[R_H]$ in Au is consistent with the stronger frequency dependence of Re$[R_H]$ in Au when compared to Cu. The sign of Im$[R_H]$ is consistent with the relative magnitudes of γ_{xy} and γ_{xx} [see Eqs. (A11) and (A12b)], as found from a comparison of σ_{xx} with θ_H. Indeed, $\gamma_{xx} \neq \gamma_{xy}$ is due to anisotropic scattering, and gives the most revealing information about the anisotropy of the scattering.

In the case of the inverse Hall angle the dc value θ_H^{-1} is in good agreement with Re$[\theta_H^{-1}]$ in the MIR. However, this is also fortuitous since the asymptotic expression [Eq. (A10)] is not valid at low frequency because of the anisotropy of the scattering on the FS. Moreover, even for isotropic scattering, the ac value of Re$[\theta_H^{-1}]$ should be larger because of phonon scattering at high frequencies. Therefore, it appears that the anisotropy effects and the inelastic scattering effects nearly cancel in this case.

From σ_{xx} we deduce that the dc γ_{xx} is smaller than the infrared γ_{xx}. This is expected both from anisotropy of the scattering and its frequency dependence. The effect of anisotropy follows from the general result that $\langle 1/\tau\rangle\langle\tau\rangle \geq 1$ for averages over the FS, since $\rho_{\text{dc}} \sim \langle\tau\rangle^{-1}$ [Eq. (1.1a)] and

$\gamma_{xx} \sim \langle \tau^{-1} \rangle$ [Eq. (A4a)]. The effect of anisotropic scattering should be comparable to that observed in the Hall coefficient or the difference between γ_{xx} and γ_{xy}. Enhanced electron-phonon scattering in the MIR is also expected due to phonon emission at low temperatures which cannot occur for dc excitation. The phonon emission component to the MIR scattering rate is estimated to be approximately 5%.[22] The frequency dependence due to anisotropy and electron-phonon interaction is quantitatively consistent with the difference between the MIR and dc γ_{xx}.

V. CONCLUSION

We have demonstrated a MIR photoelastic polarization modulation technique that can be used to obtain the complex MIR Hall conductivity in thin-film metals. The Hall frequencies obtained from these measurements are consistent with band theory, while the Hall scattering rates are consistently lower than those predicted from Drude analysis of zero-magnetic-field transmittance measurements. This difference can be explained qualitatively in terms of the difference in Fermi velocities, and hence the difference in scattering rates, for carriers in the neck and belly regions of the FS. The neck and belly regions contribute differently to σ_{xx} and σ_{xy}, which can account for the difference in γ_H and γ_{xx}. We hope that further band-structure calculations will be made to better quantify these arguments. MIR Hall angle measurements have provided a sensitive probe of the FS anisotropy in thin-film metals, and since a number of theories[6,7] predict an anisotropic FS in high-temperature superconductors, this technique may be useful for studying these less conventional materials.

ACKNOWLEDGMENTS

This work was supported in part by NSF grant DMR-9705129 and by funding from the NSA.

APPENDIX: THEORETICAL BACKGROUND FOR THE AC HALL EFFECT

In this appendix, we discuss the magnetoconductivity tensor within Fermi-liquid theory[23] and the relaxation-time approximation. These results are useful for analyzing the experimental data. Applying the small-angle approximation $\tan\theta_H \approx \theta_H$, the sum rule on θ_H is[10]

$$\int_0^\infty \mathrm{Re}[\,\theta_H] d\omega = \frac{\pi}{2}\omega_H . \tag{A1}$$

Since ω is greater than the carrier relaxation rates in the experiment discussed in this paper, it is useful to consider the asymptotic forms of the magneto-optical response functions for large $\omega\tau$. For large $\omega\tau$,

$$\tilde{\tau}(k) = \frac{1}{\dfrac{1}{\tau(k)} - i\omega} = \frac{i}{\omega} + \frac{\gamma(k)}{\omega^2} + \cdots , \tag{A2}$$

where $\gamma(k) = 1/\tau(k)$ is the k-dependent scattering rate on the FS. The limiting high-frequency behavior of the conductivity tensor in Eqs. (1.1a) and (1.1b) becomes

$$\sigma_{xx} = \sigma_{xx}^{\infty}\left(1 - i\frac{\gamma_{xx}}{\omega} + \cdots\right), \tag{A3a}$$

$$\sigma_{xy} = \sigma_{xy}^{\infty}\left(1 - 2i\frac{\gamma_{xy}}{\omega} + \cdots\right). \tag{A3b}$$

γ_{xx} and γ_{xy} are different averages of the scattering over the FS given by

$$\gamma_{xx} = \frac{\oint_{\mathrm{FS}} dS |\mathbf{v}(k)|\,\gamma(k)}{\oint_{\mathrm{FS}} dS |\mathbf{v}(k)|}, \tag{A4a}$$

$$\gamma_{xy} = \frac{\oint_{\mathrm{FS}} dS\,\gamma(k)\mathbf{e_z}\cdot\left[\mathbf{v}(k)\times\dfrac{d\mathbf{v}(k)}{dk}\right]}{\oint_{\mathrm{FS}} dS\,\mathbf{e_z}\cdot\left[\mathbf{v}(k)\times\dfrac{d\mathbf{v}(k)}{dk}\right]}. \tag{A4b}$$

σ_{xx}^{∞} and σ_{xy}^{∞} are given by

$$\sigma_{xx}^{\infty} = \frac{i\omega_p^2}{4\pi\omega}, \tag{A5a}$$

$$\sigma_{xy}^{\infty} = -\frac{\omega_p^2\omega_H}{4\pi\omega^2}, \tag{A5b}$$

where ω_p and ω_H are the plasma frequency and Hall frequency, respectively, given by integrals over the FS defined below where we have assumed cubic symmetry and used the weak-field approximation

$$\omega_p^2 = \frac{e^2}{2\pi^2\hbar}\oint_{\mathrm{FS}} dS|\mathbf{v}|, \tag{A6}$$

$$\omega_H = \frac{eB}{\hbar c}\frac{\oint_{\mathrm{FS}} dS\,\mathbf{e_z}\cdot\left[\mathbf{v}\times\dfrac{d\mathbf{v}}{d\mathbf{k}}\right]}{\oint_{\mathrm{FS}} dS[\mathbf{v}]}. \tag{A7}$$

Consequently, the asymptotic forms of θ_H and the Hall coefficient R_H are

$$\theta_H^{\infty} = \frac{i\omega_H}{\omega}, \tag{A8}$$

$$R_H^{\infty} = \frac{4\pi\omega_H}{\omega_p^2}. \tag{A9}$$

Keeping the first-order terms in $\tilde{\tau}$ in Eqs. (A3a) and (A3b), one obtains the asymptotic expansions for the inverse Hall angle θ_H^{-1} and Hall coefficient R_H,

$$\theta_H^{-1} = \frac{-i\omega}{\omega_H} + \frac{\gamma_H}{\omega_H} + O\left(\frac{i}{\omega}\right) + O\left(\frac{1}{\omega^2}\right) + \cdots , \tag{A10}$$

$$R_H = \frac{\sigma_{xy}}{\sigma_{xy}^2} = \frac{4\pi\omega_H}{\omega_p^2 B}\left[1 + \frac{i}{\omega}\gamma_R + O\left(\frac{1}{\omega^2}\right) + O\left(\frac{i}{\omega^3}\right) + \cdots\right], \tag{A11}$$

where B is the magnetic field, and

$$\gamma_H \equiv 2\gamma_{xy} - \gamma_{xx} \tag{A12a}$$

$$\gamma_R \equiv 2(\gamma_{xx} - \gamma_{xy}). \tag{A12b}$$

Equation A10 for θ_H^{-1} is particularly useful since the scattering effects and ω_H can be readily separated. Furthermore, the high-frequency asymptotic form is seen to reduce to the simple Drude form of Eq. (1.3). Also, it is seen that R_H becomes frequency dependent only when the scattering rate is not constant on the FS. This follows from either Eq. (A11), where the leading frequency dependent term is proportional to $\gamma_R = 2(\gamma_{xx} - \gamma_{xy})$ (which is zero for isotropic scattering), or in Eqs. (1.1a) and (1.1b) where a k-independent γ can be taken out of the integrals and exactly cancels in the ratio $\sigma_{xy}/\sigma_{xx}^2$.

These expressions can be extended to include frequency-dependent, inelastic scattering in the memory function formalism.[24] In this case $\gamma(k) - i\omega$ is replaced with $\Gamma(k,\omega) - i\Sigma(k,\omega) - i\omega = \Gamma(k,\omega) - i\omega[1 + \lambda(k,\omega)]$, where Γ and Σ are the real and imaginary parts of the memory function, respectively, and $\lambda(k,\omega)$ is the mass enhancement factor. Simple expressions can be obtained only for k-independent scattering. In this case it is seen that the Hall coefficient is unaffected since the scattering effects cancel. Therefore, R_H remains frequency independent. The result for θ_H^{-1} is

$$\theta_H^{-1} = \frac{\Gamma(\omega) - i\omega[1 + \lambda(\omega)]}{\omega_H}. \tag{A13}$$

Therefore, similar to the behavior of σ_{xx}, the Hall angle has the same form as in the elastic scattering case but with renormalized parameters. The real part of θ_H^{-1} gives the scattering function while the imaginary part gives the renormalized Hall frequency $\omega_H^* = \omega_H/[1 + \lambda(\omega)]$. The Hall angle sum rule is satisfied because $\lambda(\omega) \to 0$ as $\omega \to \infty$.

*Present address: Department of Physics, State University of New York at Buffalo, Buffalo, NY 14260.

[1] J. M. Harris, Y. F. Yan, and N. P. Ong, Phys. Rev. B **46**, 14 293 (1992).
[2] N. P. Ong, Phys. Rev. B **43**, 193 (1991).
[3] For example, see S. G. Kaplan, S. Wu, H.-T. S. Lihn, H. D. Drew, Q. Li, D. B. Fenner, J. M. Phillips, and S. Y. Hou, Phys. Rev. Lett. **76**, 696 (1996); J. Cerne, M. Grayson, D. C. Schmadel, G. S. Jenkins, H. D. Drew, R. Hughes, J. S. Preston, and P.-J. Kung, Phys. Rev. Lett. (to be published).
[4] Y. Tokura, A. Urushibara, Y. Moritomo, T. Arima, A. Asamitsu, G. Kido, and N. Furukawa, J. Phys. Soc. Jpn. **63**, 3931 (1994); K. Chahara, T. Ohno, M. Kasai, and Y. Kozono, Appl. Phys. Lett. **63**, 1990 (1993); R. v. Helmholt, J. Wecker, B. Holzapfel, L. Scfhultz, and K. Samwer, Phys. Rev. Lett. **71**, 2331 (1993); S. Jin, T. H. Tiefel, M. McCormack, R. A. Fastnacht, R. Ramesh, and L. H. Chen, Science **264**, 413 (1994); S. G. Kaplan, M. Quijada, H. D. Drew, D. B. Tanner, G. C. Xiong, R. Ramesh, C. Kwan, and T. Venkatesan, Phys. Rev. Lett. **77**, 2081 (1996).
[5] The generalization to lower symmetry is given in Refs. 2 and 6.
[6] A. T. Zheleznyak, V. M. Yakovenko, H. D. Drew, and I. I. Mazin, Phys. Rev. B **57**, 3089 (1998).
[7] L. B. Ioffe and A. J. Millis, Phys. Rev. B **58**, 11 631 (1998).
[8] P. W. Anderson, Phys. Rev. Lett. **67**, 2092 (1991).
[9] H. D. Drew, S. Wu, and H.-T. S. Lihn, J. Phys.: Condens. Matter **8**, 10037 (1996).
[10] H. D. Drew and P. Coleman, Phys. Rev. Lett. **78**, 1572 (1997).
[11] Model II/ZS50 from Hinds Instruments, 3175 NW Aloclek Dr., Hillsboro, OR 97124.
[12] J. Černe, D. C. Schmadel, and H. D. Drew (unpublished).
[13] K. L. Chopra, *Thin Film Phenomena* (McGraw-Hill, New York, 1969), Chap. 4.
[14] S. W. McKnight, K. P. Stewart, H. D. Drew, and K. Moorjani, Infrared Phys. **27**, 327 (1987).
[15] W. W. Schulz, P. B. Allen, and N. Trivedii, Phys. Rev. B **45**, 10 886 (1992).
[16] D. A. Papaconstantopoulos, *Handbook of the Band Structure of Elemental Solids* (Plenum Press, New York, 1986).
[17] C. Hurd, *The Hall Coefficient of Metals and Alloys* (Plenum, New York, 1972).
[18] M. A. Biondi and J. A. Rayne, Phys. Rev. **115**, 1522 (1959).
[19] B. Lengeler, W. R. Wampler, R. R. Bourassa, K. Mika, K. Wingerath, and W. Uelhoff, Phys. Rev. B **15**, 5493 (1977).
[20] J. Graefenstein, I. Mertig, E. Mrosan, V. N. Antonov, and V. L. N. Antonov, Phys. Status Solidi B **147**, 575 (1988).
[21] Z. M. Ziman, *Electrons and Phonons* (Oxford University Press, London, 1963).
[22] M. A. Biondi and J. A. Rayne, Phys. Rev. **115**, 1522 (1959).
[23] L. D. Landau, Sov. Phys. JETP **3**, 920 (1957); **5**, 101 (1957); **8**, 70 (1959).
[24] J. W. Allen and J. C. Mikkelson, Phys. Rev. B **15**, 2952 (1977).